Proceedings of 13th European Conference on Turbomachinery Fluid dynamics
Paper ID: ETC2019-418 & Thermodynamics ETC13, April 8-12, 2019; Lausanne, Switzerland

INFLUENCE OF THE NUMERICAL STRATEGY ON WALL-RESOLVED LES OF A COMPRESSOR CASCADE

D. Papadogiannis, S. Mouriaux

Safran Tech, Magny-les-Hameaux, France, dimitrios.papadogiannis@safrangroup.com

J-S Cagnone, K. Hillewaert

CENAERO, Charleroi, Belgium

F. Duchaine

CERFACS, Toulouse, France

S. Hiernaux

Safran Aero Boosters, Milmort, Belgium

ABSTRACT

The design of turbomachinery relies on inexpensive, steady-state Reynolds Averaged Navier-Stokes (RANS) predictions. However, turbomachinery flows are complex with various phenomena that can be difficult to predict with RANS. Large Eddy Simulations (LES), resolving the larger scales of turbulence, appear as an attractive alternative. However, correctly resolving turbulence is challenging as numerical schemes with the correct diffusion and dispersion properties are required. The main numerical strategy employed is the Finite Volume approach on structured or unstructured grids. More recently, Finite Element-like methods, intrinsically extending up to very high orders, such as the Discontinuous Galerkin, have emerged. However, few comparisons have been made between these approaches to assess their impact on the LES predictions of turbomachinery. In this work, wall-resolved LES of a realistic linear compressor cascade is performed using three solvers, each employing one of the strategies mentionned. The results highlight that while all three approaches predict similar overall aerodynamic losses, differences in the transition mechanisms and in the turbulent kinetic energy levels are revealed.

NOMENCLATURE

α Angle of Attack
ω Loss Coefficient
k Turbulent Kinetic Energy
CFL Courant-Friedrichs-Lewy Number
P_t Stagnation Pressure
P_s Static Pressure
τ_w Skin Friction magnitude
C Axial chord
PS Pressure Side
SS Suction Side
NSCBC Navier Stokes Characteristics Boundary Conditions
AoA Angle of Attack
DoF Degrees of Freedom
WRLES Wall-Resolved LES

INTRODUCTION

Numerical simulations are widespread in the design process of turbomachinery components for gas turbines. The current industrial state-of-the-art relies on solving the RANS equations to compute the mean variables of stationary flow fields, with a modelling of the entire turbulent spectrum. RANS is particularly adapted for simulations at or near the design point. While this method is mature and computationally affordable, it is subject to several limitations. Indeed, the flow in modern compressors and turbines exhibits high levels of unsteadiness, separations, and laminar-to-turbulent transitions, which are difficult to reliably model in RANS.

Large Eddy Simulations, aiming at resolving the most energetic length scales of the turbulent spectrum and inherently unsteady, appear very promising and can alleviate the modelling requirements of RANS. However, this suggests that the meshes and the numerical schemes employed are able to correctly resolve and transport the developing turbulence, hence present minimal diffusion and dispersion properties.

Common numerical strategies for industrial configurations use structured multi-block meshes in conjunction with 2^{nd} order Finite Volume (FV) numerical schemes. This approach is robust but can be too dissipative, while increasing the order of accuracy remains difficult on realistic geometries [1]. FV solvers using unstructured meshes are a common alternative, particularly when the geometric complexity increases. However, they can be prone to numerical difficulties and sensitive to mesh anisotropy [2]. Finite Element (FE)-like methods, such as the Discontinuous Galerkin (DG) [3], have been developed more recently to remedy these issues. These methods extend intrinsically up to very high order of accuracy and are computationally efficient and highly parallelizable on unstructured meshes. However, they may be less robust and further validations in realistic geometries are needed.

Various isolated LES studies of turbomachinery with the aforementioned strategies can be found in the literature [4, 5, 6]. However, how these methods directly compare to each other on the same test case in terms of flow predictions is an open question. To address this issue, wall-resolved LES of a realistic linear compressor cascade is performed using three solvers, each employing one of the main numerical strategies described: a traditional structured FV solver, a mixed FE/FV unstructured solver and an unstructured DG solver. The operating conditions are engine-realistic and the numerical predictions are evaluated at on and off-design angles of attack. The results are evaluated against the available experimental measurements from the Von Karman Institute. The flow fields are analyzed in detail and compared in terms of wake losses, boundary layer and blade friction profiles. The turbulent kinetic energy levels are also evaluated.

GEOMETRY

The geometry is a low-pressure compressor cascade, measured at the Von Karman Institute in a blowdown compressor cascade facility. The linear cascade is representative of modern low pressure compressor designs. During the experimental campaign, the same blade profile was tested with different solidities, at different angles of attack, and inlet Mach numbers, in order to evaluate the impact of the solidity on the onset of stall. As a result, only limited external flow measurements were conducted, focusing on aerodynamic losses [7].

In this study, a baseline configuration is evaluated, with a solidity $s = 1.38$. The Reynolds number of the flow, based on the inlet Mach number and blade chord is $Re \approx 450,000$, simulating a high subsonic configuration. The flow was simulated at two different angles of attack: $\alpha = 0^\circ$ and 10.5° (on and off-design conditions respectively). In order to reduce the compu-

tational cost of the simulations, a 2.5D domain is employed: the 2D blade profile is extruded spanwise at a length equal to 10% of the chord. This spanwise length has been evaluated as sufficient in [8, 4], by means of spanwise correlations as well as with comparisons with a domain with a spanwise length of 20% of the chord.

NUMERICAL SETUPS

In this section, a short description of the three numerical setups is presented. No inlet turbulent fluctuations were imposed because the experimentally measured value was under 0.5%. Table 1 gathers the main parameters for the numerical and mesh parameters.

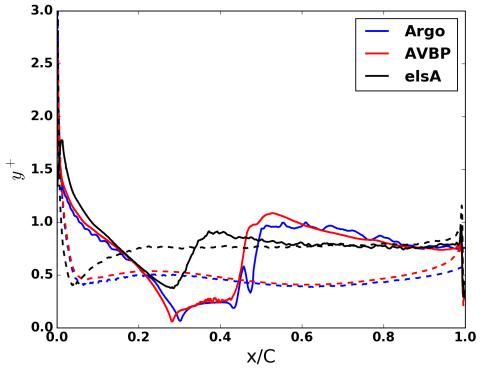

Figure 1: y^+ profile across the blade — Incidence angle = $0°$. Plain line : Suction Side, dashed line : Pression Side

Code	**Argo**	**AVBP**	**elsA**
Spatial	DG $4^{th} order$	TTG4A	Jameson
Temporal	BDF2		Gear
CFL	≈ 10	0.7	≈ 10
sgs model	none	WALE	WALE
Dofs	24.3	20	26

Table 1: Main numerical parameters

AVBP

AVBP is an unstructured compressible mixed Finite Volume/Finite Element LES solver [9], developed by CERFACS and IFP Energies Nouvelles. While originally developed for principally combustor applications, its application domains now include cascades [10], high-pressure turbines [11] and compressor flows [12, 6]. The numerical scheme employed to resolve the governing equations is the TTG4A scheme [13], 3^{rd} order in time and space. The time integration is explicit, with the timestep chosen to ensure $CFL = 0.7$, leading to $dt \approx 3.10^{-9}s$. NSCBC [14] partially non-reflective formulation is applied at the inlet and the outlet in order to avoid unwanted noise reflection at the boundaries. The sub-grid scale model employed is the WALE model, well adapted for wall bounded flows [15]

The unstructured multi-element mesh is non-extruded. Around the blade 30 prism layers enable an adequate near wall resolution, while the rest of the domain is filled with tetrahedras. The first prism layer height is selected to fullfill the criterion $Y^+ < 1$ (Fig. 1) and the height of the following layers is very gradually increased using a growth rate equal to 1.05. The aspect ratio of the prisms is kept < 8, to ensure a high element quality and a smooth transition to the tetras, an important consideration for numerical accuracy [2]. As a result, $Z^+, X^+ < 8$, a condition that largely fulfills the usual criteria for wall resolved LES. The final mesh includes 79M cells in total, corresponding to ≈ 20M of nodes.

elsA

elsA is a multi-block structured, compressible Navier-Stokes solver, developed by Onera [16]. The spatial numerical scheme used in this study is the centered 2^{nd} order Jameson scheme[17]. Numerical integration is performed using the Gear implicit method [18], second order accurate in time with a timestep $dt = 10^{-8}s$, which corresponds to $CFL \approx 10$ based on the minimum cell size at the leading edge of the cascade, and close to unity around the blade areas where turbulence develops. The sub-grid scale model employed is, as for AVBP, the WALE model. The boundary conditions are reflective, which suggests that the acoustic waves arriving at the inlet and outlet can be reflected back to the domain, hence creating numerical noise. To control this phenomenon while avoiding the use of abrupt sponge layers, far from the blade the mesh is gradually coarsened towards the inlet and outlet.

A structured O-type hexahedron mesh around the blade and H-type upstream and downstream of the blade is considered for this solver. The mesh is then extruded uniformly in the spanwise direction. The grid contains 26M cells and the spacings around the blade were selected to respect the usual guidelines for near-wall resolution i.e. $Y^+ < 1$ (Fig. 1), $X^+ < 50$, and $Z^+ < 30$ [19].

Argo

Argo is a compressible unstructured solver developed by Cenaero [20], using a Discontinuous Galerkin discretisation combined to a symmetric interior penalty formulation [21], with optimal penalty weights.

On the contrary to classical FV appraoches, the DG method allows for an arbitrary order of interpolation p. The order of convergence, measured in the L_2-norm of the error on the solution, is $p + 1$. For these calculations, an interpolation order $p = 3$ was chosen, as it offers the best ratio between accuracy and computational cost for implicit temporal integration [20]. The latter is discretized using the second-order backward-difference scheme (BDF2). At each iteration, the non-linear system is solved using Newton's method. The linear solves are carried out using a matrix-free implementation GMRES preconditionned by block-Jacobi. This implicit formulation allows to select the timestep based on the turbulence timescale, rather than on more restrictive acoustic or diffusive stability bounds. In these calculations, the time step was selected based on the inlet flow velocity and the smallest element size, and correspond to a CFL number of 10. More details can be found in [8]. No subgrid scale model is used, since DGM is an excellent candidate for ILES, as shown by studies developing the dissipation and dispersion properties of the scheme [22] and by validations on canonical cases [23].

The same mesh as in the study of [8] was employed. It is generated by a spanwise extrusion of a 2D unstructured quadratic quadrangle mesh, including a structured boundary layer around the blade with 26 layers, and ensuring a y^+ value of ≈ 1 (Fig. 10), while $x^+ \approx y^+ \approx 30$. Refinement boxes in the wake are also present. The resulting mesh includes ≈ 380000 hexadra, totalizing $\approx 24.3\ M$ degrees of freedom with the inteporlation order $p = 3$ (Table 1).

Acquisition of statistics

Once the turbulent flow is established, simulations were run with temporal statistics being accumulated during $7T_c$, with T_c the passing time over the blade expressed by $T_c = C/U_{in}$, U_{in} the inlet velocity. To accelerate the convergence, time averaged quantities were additionally spanwise averaged. The choice of the accumulation period was monitored by checking the convergence of blade and wake averaged profiles.

RESULTS

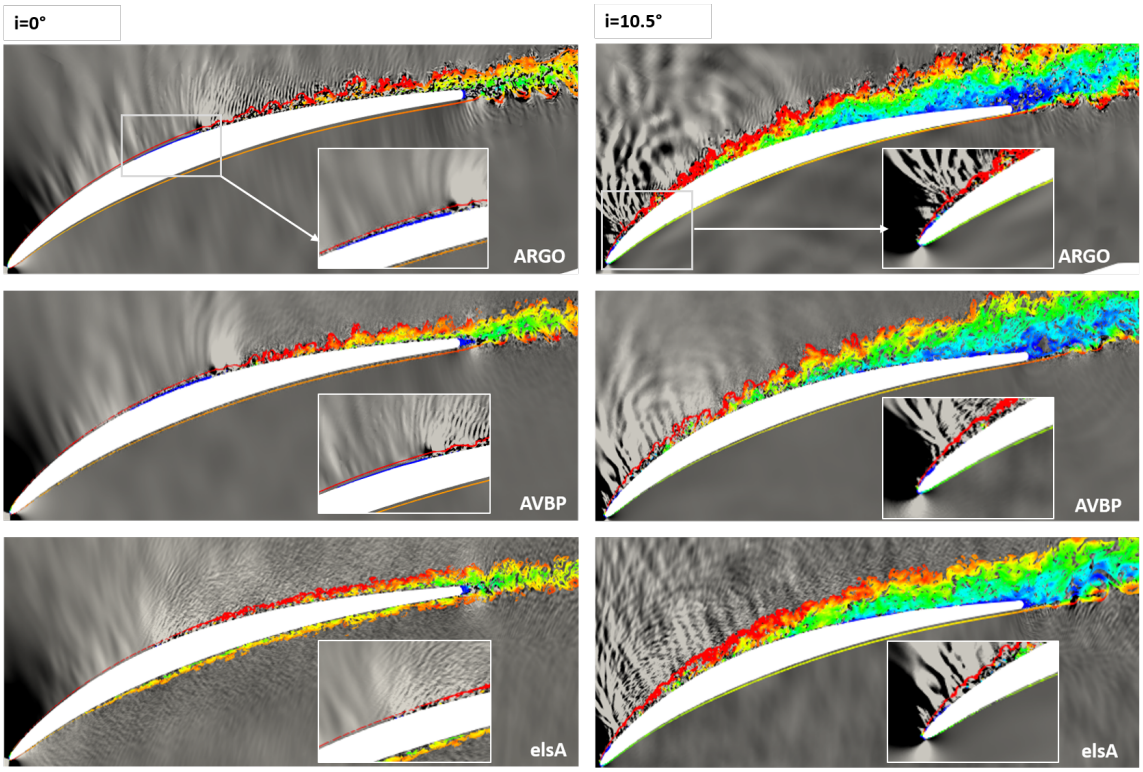

Figure 2: Instantaneous divergence field with vorticity magnitude contours colored by axial velocity. Left : Incidence angle $0°$, right $10.5°$. Top : ARGO, middle : AVBP, bottom : elsA.

Figure 2 provides a visualization of a 2D cut of the velocity divergence field with contours of the vorticity magnitude around the blade for the on (left) and off (right) design conditions. The contours are coloured such that negative axial velocity is dark blue to help illustrate the presence of any separation bubble. A qualitative comparison between the three solvers is first presented.

At incidence angle $0°$, Fig. 2 (bottom left), the elsA simulation presents a laminar-to-turbulent transition on the Suction Side (SS) at approximately 40% of the chord. On the Pressure Side (PS) transition is also visible shortly after the Leading Edge (LE). The unsteadiness of these two processes is highlighted by the generated noise observed in the divergence of the velocity, the noise levels being higher for the SS transition. On the other hand, Argo and AVBP (top and middle left respectively) provide a different flow topology : on the PS the boundary layer appears laminar, while on the SS the transition seems to be triggered by a thin laminar separation bubble (dark blue colored vorticity at the wall denoting a negative axial velocity, absent in the elsA case). These observations will be further investigated by looking at the evolution of the skin friction τ_w accross the blade (Fig. 4) in a following section.

At incidence angle $10.5°$, Fig. 2 (right), the three solvers predict a similar flow field. The SS appears fully turbulent with a separation bubble near the LE, due to the high incidence angle followed by reattachment. The boundary layer is growing rapidly, leading to higher unsteadiness and noise levels. The higher angle of attack induces increased acceleration around the

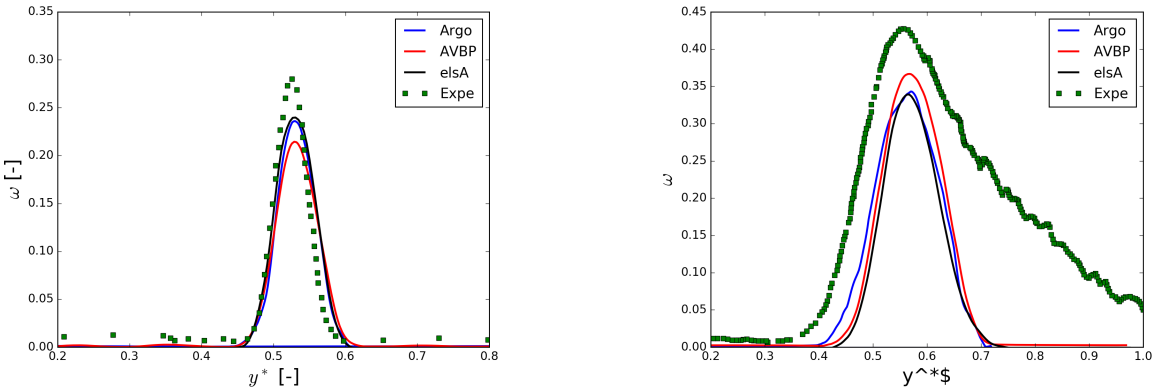

Figure 3: Profile of the wake loss coefficient ω against non-dimensional pitch y^*. Left : Incidence angle $0°$, right : Incidence angle $10.5°$. Plots are zoomed around the wake to highlight the differences between the simulations.

leading edge, with the flow reaching transonic levels and the formation of a weak shock. On the PS the boundary layer remains laminar throughout for all solvers. As for the AoA $0°$ incidence, the velocity divergence predicted by elsA shows increased levels of high frequency noise. However, it appears that at this higher angle of attack, characterized by more important potential effects, the numerical scheme and mesh differences play a less critical role on the flow phenomena predictions. The three solver converge to very similar flow structures.

Aerodynamic losses

Figure 3 compares against experiments the aerodynamic loss profiles in the wake $\omega = (p_t - p_{t,in})/(p_{t,in} - p_{in})$, with $p_{t,in}$ the total pressure and p_{in} the average static pressure at the inlet and p_t the total pressure half a chord downstream of the trailing edge.

At $\alpha = 0°$ (Fig.3 - left) the shape and thickness of the profile is well recovered by the three solvers, who however slightly underpredict the experimental loss peak. Such discrepancies between high-fidelity simulations and experimental measurements of cascades is commonly found in the literature [24]. Only minor differences in terms of peak and thickness are found between the three numerical approaches. This implies the differences on the transition mechanisms highlighted in Fig. 2 have a limited influence on a more macroscopic quantity such as overall losses. At $\alpha = 10.5°$ the non-symmetric form observed in the experiments is not captured by any of the three solvers. This consistent discrepancy, along with the non-symmetric form of the experimental loss profile, indicates that the hypothesis of a spanwise periodicity is likely not verified in the experiment. A possible cause is the presence of a corner separation that affects the mid-span flow, a common ocurrence in similar compressor cascades at off-design angles of attack [25]. Such a phenomenon is induced by the presence of the lateral walls that are not present in the simulated 2.5D domain and would thus require a full 3D geometry. However, to validate this explanation requires spanwise maps of the loss coefficient, which are unfortunately not available for this angle of attack. Beyond this inconsistency, the three simulations appear to agree rather well between them with only minor differences on the wake peak loss as well as on the thickness, with AVBP having the highest peak loss only by small margin.

Skin friction and boundary layer profiles around the blade

To further characterize the prediction of the transition mechanisms, the evolution of the skin friction magnitude across the blade is plotted in Fig. 4, at $\alpha = 0°$ (left) and $\alpha = 10.5°$ (right). To complete the analysis, wall normal profiles of the tangential velocity are plotted at different stations accross the chord on the suction side (Fig. 5). The stations are chosen to correspond to areas of particular interest and/or boundary layer regime change. The skin friction magnitude profiles have been normalized by $max(\tau_w)$ for the AVBP case at $\alpha = 0°$, the nomarlized variable depicted as $\tilde{\tau_w}$. The boundary layer velocity profiles have been normalized by a consistent value in order to fit in the plots.

On-design point

The skin friction magnitude profile, Fig. 4-(left), highlights the differences in the transition mechanisms between the three solvers. As seen in Fig. 2, Argo and AVBP exhibit flow separation on the SS at $x/C \approx 0.3$, while elsA directly transitions at a smilar location. This is indicated by the elsA friction magnitude which does not reach 0 before the characteristic friction increase occurs. Fewer differences appear between AVBP and ARGO. In the Argo case, the boundary layer appears to reattach while the flow is still laminar, as indicated by skin friction magnitude reaching 0 at $x/C = 0.42$, and transition occurs shortly afterwards. AVBP seems to predict a laminar-to-turbulent transition occuring within the separation bubble, as suggested by the steep skin friction magnitude increase without signs of prior reattachment. This interpretation is further confirmed by observing the boundary layer velocity profiles at three nearby stations (at 0.4, 0.5 and 0.6 of the axial chord), Fig. 2. At $x/C = 0.4$, elsA shows a typical turbulent boundary layer while Argo and AVBP exhibit a thin flow separation. At $x/C = 0.5$, AVBP is still separated while Argo seems to show an attached laminar profile, with velocity gradients less steep compared to the turbulent elsA profile. Further downstream, at $x/C = 0.6$, all three codes show similar profiles and similar boundary layer thicknesses. On the PS of the blade, the skin friction, Fig. 4-left, depicts a more straightforward flow picture: both Argo and AVBP show a laminar boundary layer with an excellent match of the profiles, while elsA shows laminar-to-turbulent transition near the leading edge with a minor skin friction increase past the transition point, hence confirming the observations on the snapshots in Fig. 2.

These results illustrate well the very high sensitivity of natural transition to the numerical properties and meshing strategy employed. Despite having three WRLES that match all the classic resolution criteria, differences on the predicted flow mechanisms are highlighted. The various dissipation/dispersion properties of the schemes, combined with the different types of elements, result in different ways in which the solvers develop the fluctuations susceptible to trigger transition. The solver elsA, with a second order numerical scheme on structured hexahedral meshes, allows unstable modes to develop within the boundary layer that trigger directly the transition on both sides of the blade. The two unstructured simulations, despite the higher order schemes used, lack such instabilities leading to transition via a separation bubble. Separation bubbles have been commonly observed and characterized in low-pressure turbine cascades, such as the T106 [26**?**] but their presence in realistic compressors at high Reynolds bumbers is less reported. The few studies in the literature exhibiting a separation bubble focus either on lower Reynolds numbers [27] or on cases with high free-stream turbulence [28], hence comparisons can be difficult. Nonetheless, in the case of [28], that is of similar Reynolds number, a separation bubble of similar size and at a similar location is observed at the suction side of the blade. It is important to note that in the absence of incoming turbulence and/or strong potential

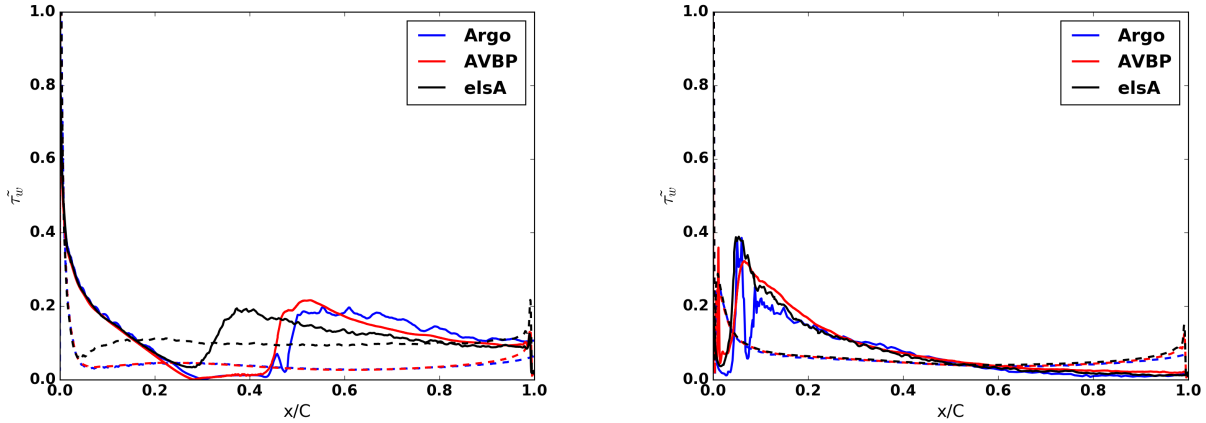

Figure 4: Axial blade profile of the normalized skin friction magnitude $\tilde{\tau}_w$ against x/C. Left : Incidence angle $0°$, right : incidence angle $10.5°$. Plain line : Suction Side, dashed line : Pression Side

effects, transition requires a very fine resolution of the modes triggering it [29], which only a DNS is likely to correctly characterize in this case. Finer measurements would also help but to the authors' knowledge, such fine experimental databases on realistic turbomachinery cascades are not available.

Off-design point

At the off-design point, the finlet flow presents a higher incidence of $10.5°$, usually resulting in separation bubbles or complete flow separation on the SS, as well as transonic velocities around the LE. The skin friction profiles are displayed in Fig. 4-(right). All simulations predict a laminar separation bubble on the SS. The position and size of the bubble appear to vary only slightly. Then all solvers indicate a transition to turbulence within the bubble and then a fully turbulent boundary layer. The strong pressure gradients result in a more straigthforward flow structures to predict, so that the three solvers converge to a similar flow picture. This conclusion is further confirmed by the boundary layer velocity profiles in Fig. 5-(bottom). Contrary to the on-design angle, the stations chosen to show the profiles are cloaser to the leading edge, as most interesting phenomena occur in this area. At $x/C = 0.1$, both elsA and Argo are already reattached as indicated by the turbulent velocity profile while AVBP is on the verge of reattachment with a very small negative velocity observed very close to the wall. Further downstream, all three solvers depict a very similar velocity profile and boundary layer thickness. On the PS of the blade, the skin friction magnitude indicates that all solvers predict a laminar boundary layer with a smooth skin friction magnitude profile and the absence of any peaks characteristic of transition.

Turbulence around the blade

A last point of comparison between the three numerical strategies is the turbulence developing around the blade. The Turbulent Kinetic Energy (TKE) levels in particular play an important role in the aerodynamic losses. Figure 6 presents the TKE around the blade for the on and off-design points (left and right) for the three solvers respectively.

For incidence angle = $0°$, AVBP depicts high levels of overall TKE, with most of it gener-

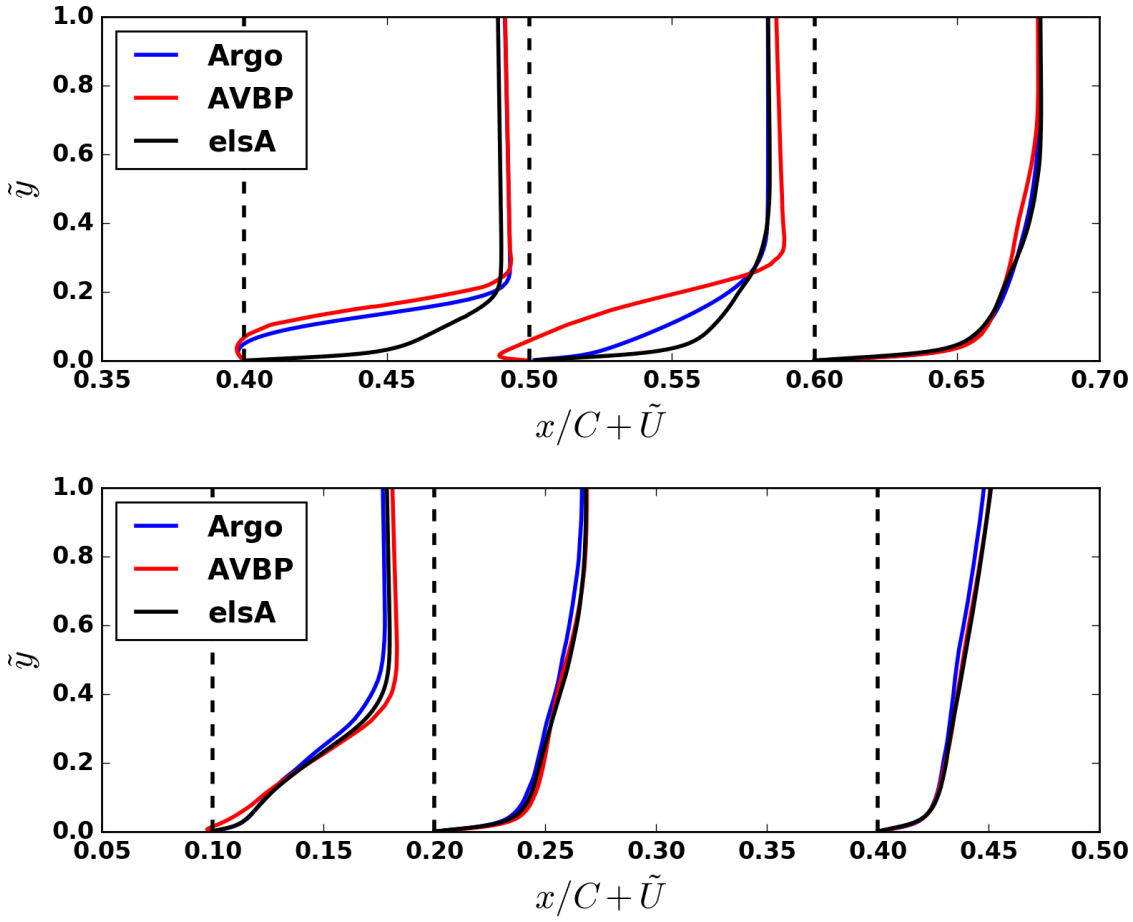

Figure 5: Velocity profile across the normal direction to the blade - Top : Incidence angle $0°$, bottom : Incidence angle $10.5°$

ated around the separation bubble. ARGO shows a similar picture with maximum TKE levels slightly downstream and in a narrower zone compared to AVBP, due to the transition occuring after reattachment. The major difference lies with the elsA simulation : as it predicts a direct transition mechanism, the maximum TKE levels are much decreased compared to AVBP and Argo, which predict a separation before the transition. Similar overall levels downstream of the blade are however observed. This indicates that while the transition mechanisms are different, the overall turbulence downstream, where losses are measured, is similar and explain the good agreement between the overall loss profile.

At the off-design incidence angle, the three solvers globally present the same flow picture, with elsA showing reduced levels of TKE. In this case, most of the fluctuations are produced by the separation near the leading edge, while further downstream the TKE profiles are diffused following the growth of the boundary layer thickness. The PS indicates very low TKE levels for all solvers.

An interesting point is that TKE fields are not as smooth as for the on-design angle towards the trailing edge. A longer averaging time might be required to achieve the convergence of the temporal statistics within the thicker boundary layer, where the velocity is decreased. As a result, running the simulation for a longer physical time will likely improve the averages within the boundary layer and smoothen the field further. Nonetheless, it allows in this case useful qualitative comparisons and combined with the spanwise averaging that is usual in such cases, it is sufficient for statistically stationary fields of the lower order quantities, such as losses and velocities.

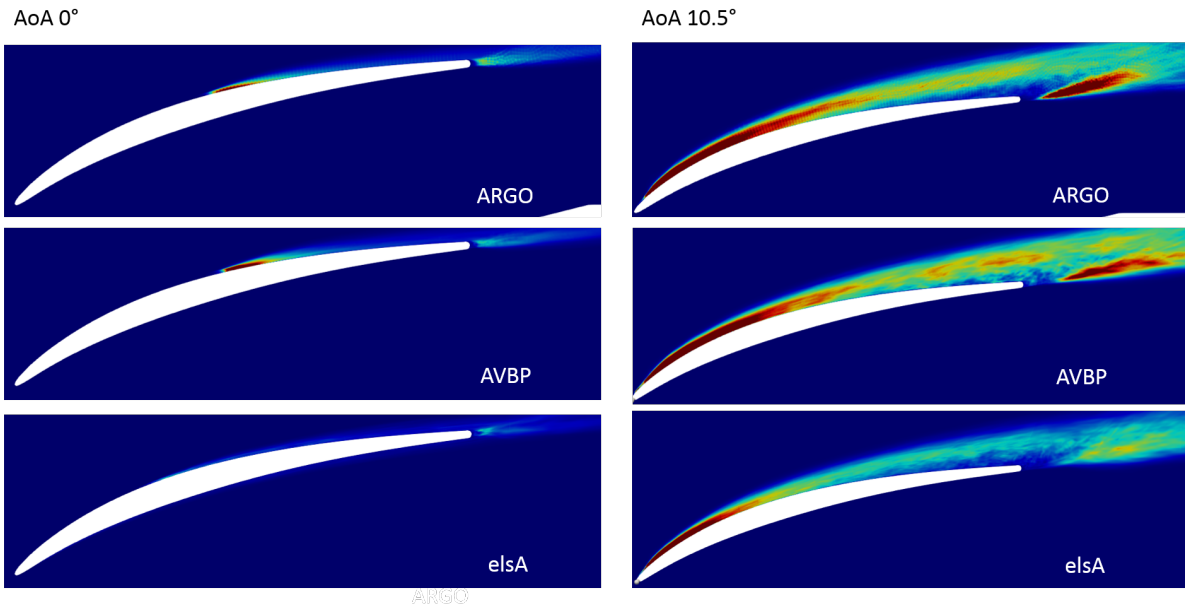

Figure 6: Cut of averaged TKE fields . Left : incidence angle $0°$, right incidence angle $10.5°$. Top : ARGO, middle : AVBP, bottom : elsA.

CONCLUSIONS

The results of this paper highlight that the numerical strategy employed in high-fidelity WRLES of turbomachinery cascades can have an important impact on the predicted flow fields,

notably due to its influence on the mechanisms of laminar-to-turbulent transition.

1. All three numerical strategies predict similar aerodynamic losses and match the experimental values relatively well for the on-design angle of attack.

2. For the off-design condition, there is potentially the effect of 3D structures due to the laterals walls that cannot be captured by a 2.5D domain.

3. At on-design angle of attack, where the flow is fully attached, the three solvers provide different transition mechanisms on the suction side of the blade. On the pressure side, Argo and AVBP predict a laminar flow field while elsA predicts transition near the leading edge.

4. At off-design angle of attack, all flow solvers converge to similar flow phenomena, with a laminar separation bubble due to high incidence leading to transition and reattachment.

5. The turbulent kinetic energy levels are similar for all three solvers downstream of the blade. However, their repartitioning around the blade is different, notably due to the varying transition mechanisms.

Regarding the outlook of this study, a DNS of this configuration could allow to determine and analyze in depth the intricate laminar-to-turbulent transition around the cascade, notably for the on-design point. Finally, anlayzing the behavior of the different numerical approaches in the presence of incoming turbulent fluctuations is a very interesting perspective as several engine components work under the influence of strong incoming turbulence.

ACKNOWLEDGEMENTS

The authors would like to thank Mr. Jagadeesh Movva for his help with the boundary layer post-processing. Part of this work was performed using computational resources granted from GENCI/CINES in the supercomputer OCCIGEN (project A0042A10465). The authors would also like to thank Safran Aero Boosters for the permission to publish these results.

References

[1] J.A. Ekaterinaris. High-order accurate, low numerical diffusion methods for aerodynamics. *Progress in Aerospace Sciences*, 41(3-4):192–300, 2005.

[2] L.M. Segui Troth. *Multiphysics coupled simulations of gas turbines*. PhD thesis, 2017.

[3] B. Cockburn and C.W. Shu. Runge–kutta discontinuous galerkin methods for convection-dominated problems. *Journal of scientific computing*, 16(3):173–261, 2001.

[4] J. Movva, D. Papadogiannis, and S. Hiernaux. Assessment of wall modelling for large eddy simulations of turbomachinery. In *ASME Turbo Expo 2018: Turbomachinery Technical Conference and Exposition*, pages V02CT42A022–V02CT42A022. American Society of Mechanical Engineers, 2018.

[5] C. Carton de Wiart, K. Hillewaert, E. Lorriaux, and G. Verheylewegen. Development of a discontinuous galerkin solver for high quality wall-resolved/modelled dns and les of practical turbomachinery flows on fully unstructured meshes. In *ASME Turbo Expo 2015: Turbine Technical Conference and Exposition*, pages V02BT39A035–V02BT39A035.

[6] D. Papadogiannis and X. Garnaud. Unstructured large eddy simulations of the transonic compressor rotor 37. In *23rd AIAA Computational Fluid Dynamics Conference*, page 3612, 2017.

[7] J. Sans, J-F. Brouckaert, and S. Hiernaux. Experimental and numerical investigations of the solidity effect on a linear compressor cascade. In *Proc. of the ASME Turbo Expo 2015*. American Society of Mechanical Engineers, 2015.

[8] J. Cagnone, M. Rasquin, K. Hillewaert, and S. Hiernaux. Large eddy simulation of a low-pressure compressor cascade at high incidence. In *Proc. of the 12th European Conference on Turbomachinery*, 2017.

[9] T. Schonfeld. Steady and unsteady flow simulations using the hybrid flow solver avbp. *AIAA journal*, 37(11):1378–1385, 1999.

[10] E. Morata, N. Gourdain, F. Duchaine, and L. Gicquel. Effects of free-stream turbulence on high pressure turbine blade heat transfer predicted by structured and unstructured les. *Int. J. of Heat and Mass Transfer*, 55(21):5754–5768, 2012.

[11] D. Papadogiannis, F. Duchaine, L. Gicquel, G. Wang, and S. Moreau. Effects of subgrid scale modeling on the deterministic and stochastic turbulent energetic distribution in large-eddy simulations of a high-pressure turbine stage. *J. of Turbomachinery*, 138(9):091005, 2016.

[12] J. Laborderie, F. Duchaine, O. Vermorel, L. Gicquel, and S. Moreau. Application of an overset grid method to the large eddy simulation of a high-speed multistage axial compressor. In *Proc. of the ASME Turbo Expo 2016*. American Society of Mechanical Engineers, 2016.

[13] J. Donea. A taylor–galerkin method for convective transport problems. *International Journal for Numerical Methods in Engineering*, 20(1):101–119, 1984.

[14] T. Poinsot and S. Lele. Boundary conditions for direct simulations of compressible viscous flows. *J. of Computational Physics*, 101(1):104–129, 1992.

[15] F. Nicoud and F. Ducros. Subgrid-scale stress modelling based on the square of the velocity gradient tensor. *Flow, Turb. and Combustion*, 62(3):183–200, 1999.

[16] L. Cambier, S. Heib, and S. Plot. The onera elsa cfd software: input from research and feedback from industry. *Mechanics & Industry*, 14(3):159–174, 2013.

[17] A. Jameson, W. Schmidt, E. Turkel, et al. Numerical solutions of the euler equations by finite volume methods using runge-kutta time-stepping schemes. In *14th Fluid and Plasma Dynamics Conference*. American Institute of Aeronautics and Astronautics, 1981.

[18] C.W. Gear. The automatic integration of ordinary differential equations. *Communications of the ACM*, 14(3):176–179, 1971.

[19] H. Choi and P. Moin. Grid-point requirements for large eddy simulation: Chapman's estimates revisited. *Physics of fluids*, 24(1):011702, 2012.

[20] K. Hillewaert. *Development of the discontinuous Galerkin method for high-resolution, large scale CFD and acoustics in industrial geometries*. Presses univ. de Louvain, 2013.

[21] D.N. Arnold, F. Brezzi, B. Cockburn, and L.D. Marini. Unified analysis of discontinuous galerkin methods for elliptic problems. *SIAM journal on numerical analysis*, 39(5):1749–1779, 2002.

[22] P.E. Bernard et al. *Discontinuous Galerkin methods for geophysical flow modeling*. PhD thesis, PhD thesis, Université catholique de Louvain, 2008.

[23] C. Carton de Wiart, K. Hillewaert, and P. Geuzaine. Dns of a low pressure turbine blade computed with the discontinuous galerkin method. In *ASME Turbo Expo 2012: Turbine Technical Conference and Exposition*, pages 2101–2111. American Society of Mechanical Engineers, 2012.

[24] *DNS of Low-Pressure Turbine Cascade Flows With Elevated Inflow Turbulence Using a Discontinuous-Galerkin Spectral-Element Method*, Seoul, Korea, 2016.

[25] W. Ma, X. Ottavy, F. Leboeuf, and F. Gao. Experimental investigations of corner stall in a linear compressor cascade. In *Proc. of the ASME Turbo Expo*, 2011.

[26] J. Michalek, M. Monaldi, and T. Arts. Aerodynamic performance of a very high lift low pressure turbine airfoil (t106c) at low reynolds and high mach number with effect of free stream turbulence intensity. *Journal of Turbomachinery*, 134(6):061009, 2012.

[27] TA Zaki, JG Wissink, PA Durbin, and W Rodi. Direct computations of boundary layers distorted by migrating wakes in a linear compressor cascade. *Flow, turbulence and combustion*, 83(3):307–322, 2009.

[28] J. Leggett, S. Priebe, R. Sandberg, V. Michelassi, and A. Shabbir. Detailed investigation of rans and les predictions of loss generation in an axial compressor cascade at off design incidences. In *Proc. of the ASME Turbo Expo 2016*. American Society of Mechanical Engineers.

[29] L Jecker, O Vermeersch, H Deniau, E Croner, and G Casalis. A laminar kinetic energy model based on the klebanoff-mode dynamics to predict bypass transition. *European Journal of Mechanics-B/Fluids*, 2018.